Research article

Grading of glioma tumors using digital holographic microscopy

Violeta L. Calin [a,b], Mona Mihailescu [c,d,*], George E.D. Petrescu [e,f],
Mihai Gheorghe Lisievici [g], Nicolae Tarba [h], Daniel Calin [a],
Victor Gabriel Ungureanu [a], Diana Pasov [g], Felix M. Brehar [e,f], Radu M. Gorgan [e,f],
Mihaela G. Moisescu [a,b,**], Tudor Savopol [a,b]

[a] Biophysics and Cellular Biotechnology Dept., Faculty of Medicine, University of Medicine and Pharmacy Carol Davila, 8 Eroii Sanitari Blvd., 050474, Bucharest, Romania
[b] Excellence Center for Research in Biophysics and Cellular Biotechnology, Faculty of Medicine, University of Medicine and Pharmacy Carol Davila, 8 Eroii Sanitari Blvd., 050474, Bucharest, Romania
[c] Digital Holography Imaging and Processing Laboratory, Physics Department, Faculty of Applied Sciences, National University for Science and Technology Politehnica Bucharest, 313 Splaiul Independentei, 060042, Bucharest, Romania
[d] Centre for Fundamental Sciences Applied in Engineering, National University for Science and Technology Politehnica Bucharest, 313 Splaiul Independentei, 060042, Bucharest, Romania
[e] Department of Neurosurgery, "Bagdasar-Arseni" Clinical Emergency Hospital, 12 Berceni st., 041915, Bucharest, Romania
[f] Department of Neurosurgery, Faculty of Medicine, University of Medicine and Pharmacy Carol Davila, 8 Eroii Sanitari Blvd., 050474, Bucharest, Romania
[g] Department of Pathology, "Bagdasar Arseni" Clinical Emergency Hospital, 12 Berceni st., 041915, Bucharest, Romania
[h] Doctoral School of Automatic Control and Computers, National University for Science and Technology Politehnica Bucharest, 313 Splaiul Independentei, 060042, Bucharest, Romania

ARTICLE INFO

ABSTRACT

Gliomas are the most common type of cerebral tumors; they occur with increasing incidence in the last decade and have a high rate of mortality. For efficient treatment, fast accurate diagnostic and grading of tumors are imperative. Presently, the grading of tumors is established by histopathological evaluation, which is a time-consuming procedure and relies on the pathologists' experience. Here we propose a supervised machine learning procedure for tumor grading which uses quantitative phase images of unstained tissue samples acquired by digital holographic microscopy. The algorithm is using an extensive set of statistical and texture parameters computed from these images. The procedure has been able to classify six classes of images (normal tissue and five glioma subtypes) and to distinguish between gliomas types from grades II to IV (with the highest sensitivity and specificity for grade II astrocytoma and grade III oligodendroglioma and very good scores in recognizing grade III anaplastic astrocytoma and grade IV glioblastoma). The procedure bolsters clinical diagnostic accuracy, offering a swift and reliable means of tumor characterization and grading, ultimately the enhancing treatment decision-making process.

* Corresponding author. Digital Holography Imaging and Processing Laboratory, Physics Department, Faculty of Applied Sciences, National University for Science and Technology Politehnica Bucharest, 313 Splaiul Independentei, 060042, Bucharest, Romania.
** Corresponding author. Biophysics and Cellular Biotechnology Dept., University of Medicine and Pharmacy Carol Davila, 8 Eroii Sanitari Blvd., 050474, Bucharest, Romania.
E-mail addresses: mona.mihailescu@upb.ro (M. Mihailescu), mihaela.moisescu@umfcd.ro (M.G. Moisescu).

1. Introduction

Among cerebral tumors, gliomas are the most common type of cancer and are characterized by a continuously increasing incidence and a high rate of mortality [1]. They represent an infiltrative type of brain tumor arising from glial cells and have clinical evolution and prognostic depending on their histological and molecular features. Gliomas are classified in four grades, from I to IV [2], the survival prognostic being directly correlated to the tumor grading at the time of diagnosis [3]. For instance, grade II gliomas are considered low-grade tumors, which have a survival expectation between 5 and 7 years and a clinical evolution characterized by a progression to a higher grade [4]. Grade IV (glioblastoma) is the most common malignant primary brain tumor and has the most aggressive clinical evolution, with a median survival of around 15 months [4], despite the multimodal treatment procedures (surgical resection, radio- and chemotherapy). The neuro-oncologist adapts the therapeutic strategy according to the tumor grading [5]. It is thus very important to have a fast and accurate grading to improve the patient's survival and life quality.

The diagnosis is raised on imaging investigations (brain CT and MRI scans which often include advanced sequences such as MR spectroscopy) and is established by histopathological exam. After being fixed, embedded in paraffin, sectioned, and stained, the tissue sample is evaluated by light microscopy, based on cytological features like cellularity, atypia mitotic activity, presence of necrosis areas and microvascular proliferations [6]. Although the sample preparation may be automatized, the histopathological evaluation is manually done, and subjected to inter-observer variability. Since 2016, by correlating the histological features with those provided by immunohistochemistry or sequencing, the World Health Organization (WHO) Classification of Central Nervous System (CNS) Tumors [3] eliminated many inadvertencies of the histological diagnostic and increased specificity by allowing a more refined classification in sub-types (i.e., astrocytoma, ependymoma, oligodendroglioma). For instance, the presence of gene mutations of isocitrate dehydrogenase influences the prognosis and is currently included in the diagnosis guidelines, being routinely evaluated [7]. Moreover, the latest WHO 2021 Classification of CNS Tumors further promoted the role of molecular biomarkers in defining the tumor grading and subsequently establishing the prognosis [8]. Also, more advanced techniques such as DNA-methylation are being used to improve the diagnostic accuracy [9].

However, molecular and histopathological methods present some weaknesses, especially related to their costs and duration. In the case of histopathological methods, the preparation protocol is a multi-step and time-consuming process, requesting expensive reagents and dyes. Interpretation and decision diagnosis demand well-trained pathologists and are subjected to human bias and influenced by preparation artifacts. To overcome these shortcomings, during the recent years, digital pathology (DP) has been developed, aiming to: i) find new (digital) biomarkers able to provide an objective evaluation of the tissue sample, and ii) automatize the grading procedure by using classification algorithms.

DP consists of digitizing microscopy images of tissue slides creating large image libraries for various types of pathologies, including cancer. It endorses sharing, cooperation, education, and better management of clinical information [10]. Moreover, artificial intelligence (AI) tools can be trained on digital libraries for automatic recognition and evaluation of abnormal tissue, digital pathology combined with AI algorithms presently being seen as a powerful complementary diagnostic tool. AI makes use of two main approaches: i) *deep learning,* which is based on unsupervised feature learning and requests a large image database (well fitted to low-level tasks as object detection or segmentation), and ii) *supervised machine learning,* which is based on hand-crafted feature engineering and requests small-sized image dataset. In DP, the latter is usually implemented in close collaboration with pathologists and is considered more appropriate in case of high-level decision tasks, such as disease prognosis [11]. DP workflows performing automate detection, grading and subtyping of tumor tissues simplify and potentiate the diagnosis process [12].

Digital holographic microscopy (DHM), a modern interferometric technique from the larger family of Quantitative Phase Microscopy [13], offers 3D images of cells (either living or fixed), without staining and chemical labeling [14]. During the recent years DHM has been proved as a valuable biomedical tool in the field of hematology [15,16], oncology [17,18], pharmacology [19], infectious diseases [20–22], inflammation [23], neurology [24] and monitoring of cells response to various conditions [25]. DHM relies on the refractive index of a transparent sample, instead of characteristics resulting from staining, being a good method to monitor either attached cells or spheroids [26–28]. DHM provides a so-called quantitative phase image (QPI), which represents a map of the optical phase delay induced by the sample in the transmitted light, delay depending on both the refractive index and thickness of the sample in each image pixel [29]. DHM applied on tissue samples has also been reported [30]. It works on unstained tissue samples and allows a fast image acquisition (no scan being needed). In the case of a tissue section with constant thickness, QPI is a map of the refractive index, which in turn is directly related to the protein content [31]. It is well documented that the progression towards malignancy of cells and tissues is accompanied by abnormalities in the protein content and distribution [32]; therefore, QPIs can be used to compute optical phase biomarkers, which are related to the malignancy grade of cells and tissues [33]. DHM is thus a promising tool in the field of DP.

DHM joins other label-free optical techniques, which provide support for histopathology, such as: i) vibrational spectroscopy, used for glioma grading based on spectral fingerprint [34], ii) full field optical coherence tomography, used to classify human ovarian tissue as normal or malignant [35], iii) Raman spectroscopy, used for identification and grading of gliomas [36], iv) Spatial Light Interference Microscopy, used for characterization of tissues like prostate [37] or colonic mucosa [38] and hyperspectral imaging for brain tissue [39].

Our previously published analyses of QPI-derived optical biomarkers for malignant gliomas have correctly differentiated between two levels of malignancy, with good sensitivity and specificity [40,41]. In this work, we present an AI-driven pipeline trained and validated on a QPIs library of unstained glioma samples. The experimental results showed that our supervised machine learning procedure can distinguish between tumors of grades from II to IV. Optical fingerprints of each grade were extracted and analyzed using statistical and texture parameters. By quantifying the optical fingerprint, multi-class classifiers for automatic grading of gliomas tissues

have been trained and tested. These classifiers provide quantitative evaluation of pathological indicators, strengthening thus the clinical diagnostic decision.

2. Materials and methods

The study workflow was as follows: a tissue slide, hematoxylin and eosin (H&E) stained, was diagnosed by the pathologists and a consecutive one (thus having the same label as the H&E stained one), unstained, was used for quantitative phase image acquisition. A classification algorithm was trained and validated on these already diagnosed images. Then, the standard testing procedure of the algorithm was applied to classify a naïve set of images. This classification was then confirmed (or not) by the pathologists.

2.1. Sample selection and preparation

Tissue samples were obtained from the archives of the Department of Pathology ("Bagdasar-Arseni" Clinical Emergency Hospital) coming from patients that underwent surgery between 2015 and 2019. The study has received Institutional approval from the Ethics Committee at Bagdasar-Arseni Clinical Emergency Hospital (No. 19747/May 25, 2021). The samples were selected from patients older than 18 years, with a brain MRI and CT suggestive for glioma and a histopathological-confirmed diagnosis of glioma.

Samples were prepared using the following procedure: two consecutive slices were cut at 4 μm thickness from a tissue sample previously fixed with formalin and embedded in paraffin. The slices were placed onto microscope slides, then thoroughly deparaffinized following a standard procedure: heated in an oven (60 °C, 18 h), and passed through successive baths with alcohol (3 changes, 30 min each) and xylene (15 min). One of the two slices was stained using H&E while the other slice was left unstained. Samples were cover-slipped and mounted with xylene based mounting media. 18 pairs of stained and unstained tissue samples of gliomas of grade II to IV were obtained from 18 patients (an example of a stained and unstained pair of consecutive slices of a glioma tumor is presented in Fig. 1a.

2.2. Histological evaluation of tissue samples

Histological grading of the H&E-stained samples was independently done by two experienced pathologists. Equivalent areas on H&E slide and on its paired unstained slide (from which DHM images were to be acquired), were identified. As controls, normal brain tissue areas outside the tumor borders have been used. Since the stereotactic biopsies are performed with minimal invasiveness, the normal tissue areas, located peripheral to the tumor, were sparse and much smaller compared to tumor areas. However, a few such small areas could be used.

The following experimental groups of diffuse gliomas were constituted: normal (n0), grade II (a2 - diffuse astrocytoma, o2 - oligodendroglioma), grade III (a3 - anaplastic astrocytoma, o3 - anaplastic oligodendroglioma), and grade IV (g4 - glioblastoma).

2.3. Image acquisition

Holograms were acquired with a Lyncée Tec DHM®-R1000 digital holographic microscope (based on a Mach-Zehnder configuration, in transmission, with a vertical resolution of 2 nm), equipped with a 666 nm laser and a 20 × objective (NA = 0.85). An example of a hologram can be seen in Fig. 1b. Based on the holograms, QPIs of 750 × 750 pixels (corresponding to 235 × 235 μm) were reconstructed using the proprietary Koala® (software based on C++ and .NET). Briefly, the quantitative phase image of tissue is reconstructed following several standard mathematical steps (implying Fourier transform, Fresnel approximation to simulate propagation in near field) according to Ref. [42].
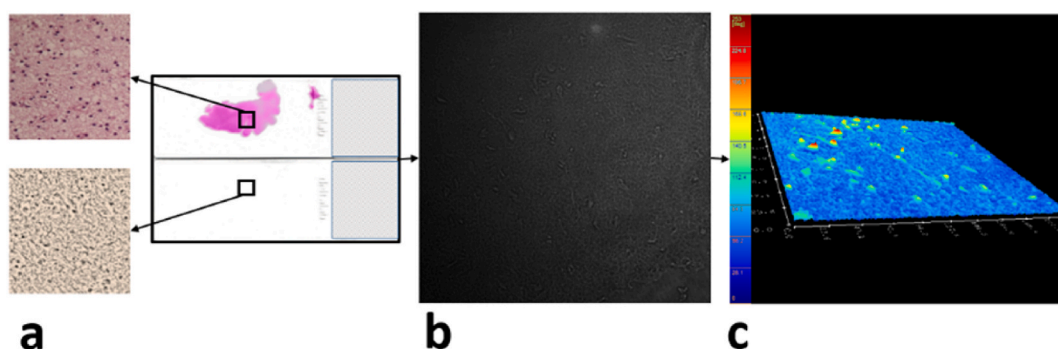
Fig. 1. Experimental procedure: a) histological slides of consecutive tissue slices, both prepared according to the standard pathological procedure (up: one was H&E stained and used for bright field microscopy examination; down: one was left unstained and used for QPI acquisition); b) recorded hologram; c) reconstructed pseudo 3D QPI in color-coded phase values. (For interpretation of the references to color in this figure legend, the reader is referred to the Web version of this article.)

A collection of 614 QPIs was obtained from the 18 unstained samples. Examples of QPIs are presented in Fig. 1c.

2.4. Image processing and analysis

A QPI represents a map of phase shift values, $\Delta\varphi(x, y)$, which depend on both the height and refractive index of the sample in each pixel of the image, according to the following equation:

$$\Delta\varphi\left(x, y\right) = \frac{2\pi}{\lambda} n(x, y) h(x, y)$$

where: λ is the laser wavelength, h is the sample thickness and n is the average refractive index of the sample in the point of (x, y) coordinates. Considering the constant thickness of tissue sections (4 μm), the phase shifts in each point are only affected by the refractive index, which in turn is proportional to the tissue protein content in those points [31]. QPIs were reconstructed by Koala®, which provides also the *.txt files to be further used as input for data processing in MATLAB 2016a (MathWorks, USA) and Python v3.9.2, using either built-in functions or custom written codes. For noise removal, a median filter with a size of five was applied on each QPI, before any subsequent computation. Several sets of parameters were computed either on the *entire image* or on *regions of interest* (ROIs). Because cellular structures induce higher phase values than the stromal matrix, only pixels with phase shift values in the 90th percentile or higher within the entire image were kept for further analysis. Regions containing more than 36 such pixels distributed in compact groups were kept, considered as cells, and defined as ROIs.

On the *entire image* the following parameters were computed: a) statistical parameters - *Mean^{2}/var*, *Skewness*, *Kurtosis*, *Mode, Phase Volume*, *Bimodality*, and *Mass Center Shift* (MCS) [17], b) texture parameters based on Gray-Level Co-Occurrence Matrix computed based on the phase values of QPIs - *Contrast*, *Energy*, *Homogeneity*, *Entropy*, *Dissimilarity*, and *Correlation,* described elsewhere [43].

On the ROIs, *local parameters* (Table 1, positions 1–15) were computed.

Pixels not selected in ROIs were considered as belonging to the stroma, for which two more *local parameters* were calculated: *anisotropy* and *gradient vector* magnitude (Table 1, positions 16–17).

All these parameters were further considered as classifiers in the automatic grading procedure of gliomas.

2.5. Machine learning

Machine learning was performed in MATLAB using the Statistics and Machine Learning Toolbox (with the Classification Learner App).

Dataset was prepared as follows.

- each QPI was attributed to a class corresponding either to normal tissue (n0) or to glioma subtypes (a2, a3, o2, o3, g4), based on the pathologist's classification of the corresponding H&E-stained slides,
- each image was then divided into four subimages, resulting 2455 sub images of 375 × 375 pixels (few sub images were discarded, due to technical reasons),
- parameters were calculated on each subimage and placed in a $n \times m$ matrix where n represents the number of parameters and m the number of subimages,
- the dataset was randomly divided into 75 % images for training and validation (the *training set* of 1842 images) and 25 % for testing (the *naïve set* of 613 images).

Table 1
Parameters calculated on ROIs and stromal component.

	Local parameter	Description
1	Roi_count	Number of individual selected ROIs on each QPI
2	Cell_percent	Number of pixels occupied by all ROIs in a QPI, expressed as percent
3	Dist	Average distance between ROI centers on each QPI
4	Slice_area	Projected area of ROIs, expressed as an average on each QPI
5	Major_axis_length	Major axis of the ellipse which can approximate the shape of a ROI, expressed as an average on each QPI
6	Minor_axis_length	Minor axis of the ellipse which can approximate the shape of a ROI, expressed as an average on each QPI
7	Eccentricity	Eccentricity of the ellipse which can approximate the shape of a ROI, expressed as an average on each QPI
8	Volume	Mean phase volume of ROIs on each QPI
9	Surface_area	Unfolded surface area of all visible faces of a ROI, expressed as an average on each QPI
10	Heights_long_axis	Average of the values of phase shift higher than the 90th percentile collected along the long axis of the ROI ellipse
11	Heights_short_axis	Average of the values of phase shift higher than the 90th percentile collected along the short axis of the ROI ellipse
12	Cell_grad	Average of the phase shift gradient moduli for a ROI expressed as a mean value for all ROIs on each QPI
13	Perimeter	Average of all segmented perimeters of each ROI, on entire QPI
14	Perimeter_div_surf_area	Ratio of ROI perimeter to the ROI slice_area
15	Adj_grad	Average of the phase shift gradient moduli for areas outside ROIs but within the smallest rectangle which fits the ROI (ROI adjacent stroma), expressed as a mean value for all ROIs adjacent stromas on each QPI
16	g	Optical anisotropy value calculated as defined in [44]
17	Stromal_grad	Average of the phase shift gradient moduli for the entire QPI except ROIs

All classifier model types available in Classification Learner App were trained on the *training set*. The performance of algorithms was evaluated by fivefold cross-validation. Good accuracies were only obtained when using support vector machine (SVM) algorithms.

The classification of glioma QPIs according to grades and subtypes represents a multiclass task. Two strategies to solve a multiclass task can be used: i) the *one-vs-one* strategy, when the multiclass task is split into one binary classification problem per each pair of classes (in this case producing 15 classification tasks by pairwise); ii) the *one-vs-all* strategy, when each class is classified against all the other classes, resulting 6 classification tasks.

The Optimizable SVM model was further used. For this model, the Optimizer Hyperparameters were: box constraint level (0.001–1000), kernel scale (0.001–1000), kernel functions (Gaussian, Linear, Quadratic and Cubic) and multiclass method (*one-vs-one* and *one-vs-all*) and the Optimizer options were: Bayesian optimization and 30 iterations. Accuracy, true positive rate, false positive rate and area under curve (AUC) were calculated from the receiver operating characteristic (ROC) curves for each of the resulting classification tasks.

An unbiased testing was done after training and validation, using the *naïve set*. The flowchart of described SVM for classification of QPIs is illustrated in Fig. 2.

2.6. Statistical analysis

Statistical tests were performed using ANOVA test (R software v4.2.3). The significance level was set at $p < 0.05$.

3. Results

3.1. QPIs library of unstained gliomas

Fig. 3 presents examples of H&E images (upper row) and QPIs (lower row) of normal tissue and grade II gliomas, while Fig. 4 presents the same categories of images, but for glioblastoma.

The main histological features observed on the H&E samples were: normal tissue presented normal cellularity and glial cells with captive neurons (Fig. 3A, upper row), grade II oligodendroglioma presented hypercellularity, uniform rounded nuclei and small, densely packed tumor cells (Fig. 3B, upper row), while grade II diffuse astrocytoma presented naked nuclei with hyperchromasia, irregular contours, mild hypercellularity and atypia (Fig. 3C, upper row).

Typical histological features were used to diagnose glioblastoma: hypercellularity with multinucleated giant cells, microvascular proliferation, pseudopalisading necrosis and necrosis with bland, acellular areas (Fig. 4A to D, upper row).

3.2. Statistical analysis of parameters computed on entire image and ROIs defined in QPIs

Significance of differences between glioma grades and subtypes, as reflected in the calculated parameters are presented in Table 2, where significant differences are marked with "1".

One can see that there are parameters which distinguish between a high number of pairs of classes (e.g., Energy and Cell_percent, which distinguish between 13 pairs of classes). On the other hand, there are pairs of classes which are differentiated by a high number of parameters: g4 vs. a2, o3 vs. a2, and o2 vs. g4 are differentiated by 25, 24, and 23 parameters, respectively.

3.3. SVM classification of QPIs

The selected optimized model was a Gaussian SVM, with kernel scale of 7.4392, box constraint level 860.24, multiclass method *one-vs-all*. This model classified the QPIs with good accuracy (Fig. 5). The training and validation set consisted of the following numbers of QPIs subimages: a2 – 325, o2 – 574, a3 – 137, o3 – 67, g4 – 619, n0 – 120.

In Fig. 5, the confusion matrix resulting from the training and validation step is presented. Four classes (a2, a3, g4, o2) were classified with accuracies above 82 %, while n0 was categorized with 71.9 % accuracy. The best categorized was a3, at 89.9 % accuracy. The o3 classification was less accurate (58.8 %).
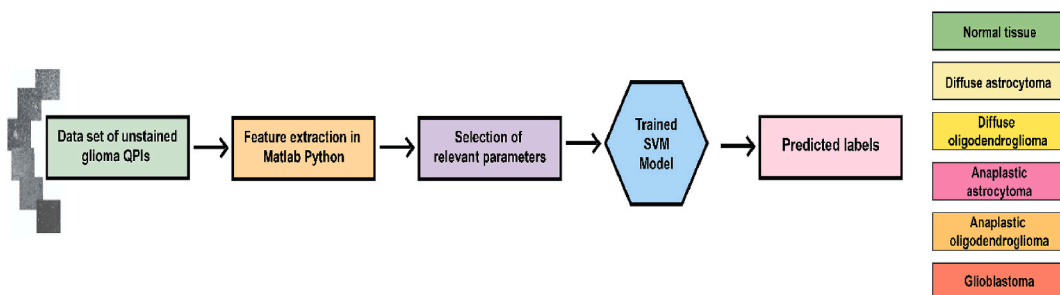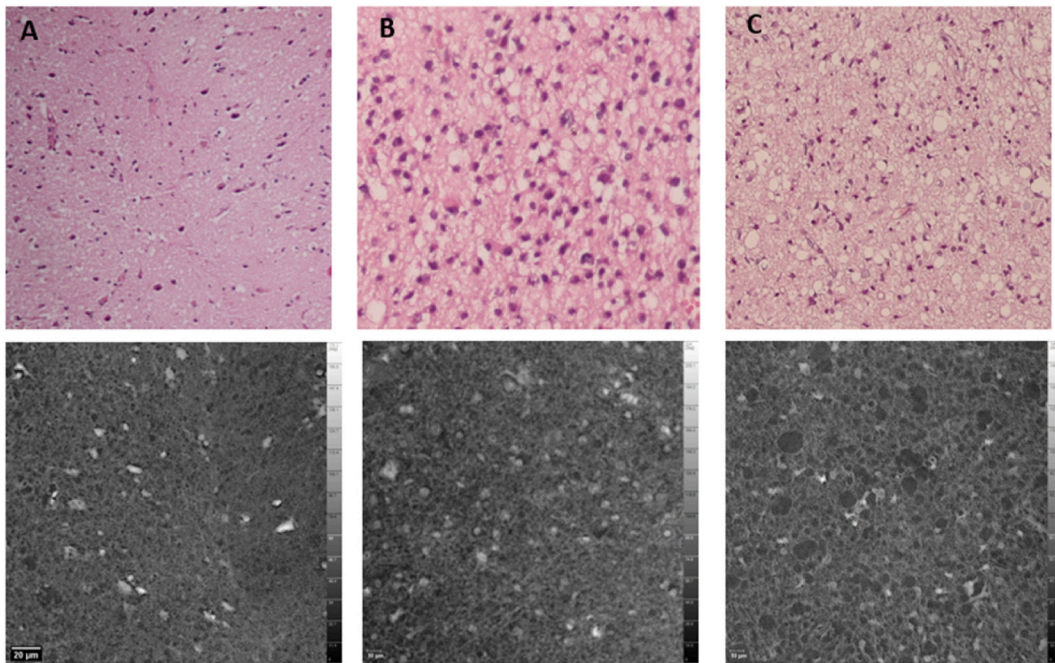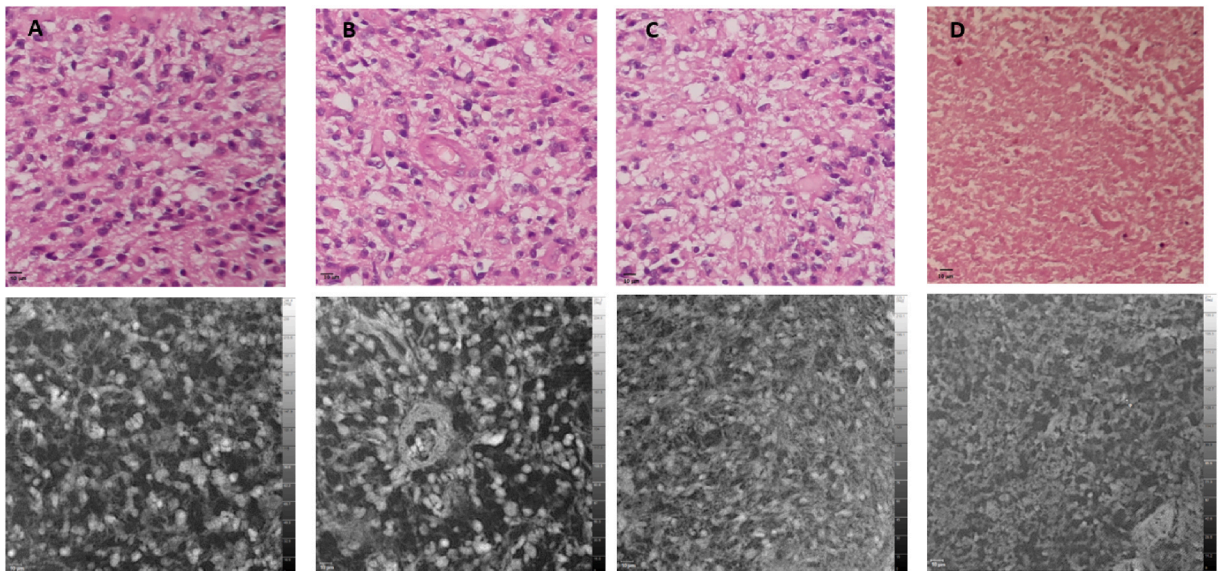

Fig. 2. Flowchart of main working steps of SVM used for classification of QPIs obtained from unstained glioma slides.

Fig. 3. Examples of H&E images (upper row) and QPIs obtained on unstained slides (lower row) of normal tissue (A) and grade II gliomas with the sub-types: oligodendroglioma (B) and diffuse astrocytoma (C).

Fig. 4. Examples of H&E images (upper row) and QPIs obtained on unstained tissues (lower row) of grade IV glioma (A to D present various histological features).

In Fig. 6 the ROC curves resulting from the testing and validation step (based on *one vs all* approach) are presented. Classes a2 and a3 were identified with the best sensitivity and specificity (AUC = 0.99 for both).

The testing step used the *naïve* set consisting in the following numbers of QPI subimages: a2 – 108, o2 – 191, a3 – 46, o3 – 23, g4 – 205, n0 – 40. The classification performances are presented in Table 3.

4. Discussion

The combination of AI algorithms and DHM has shown significant potential in addressing various biomedical tasks such as red-

Table 2
Statistical significance of differences between pairs of classes as computed for different parameters. Significant differences are marked with "1".

Parameters	g4-a2	o3-a2	o2-g4	o2-a2	o3-o2	g4-a3	n0-a2	o3-n0	a3-a2	o3-a3	o2-n0	o2-a3	n0-a3	n0-g4	o3-g4	Nb. of classes pairs recognized as different
Energy	1	1	1	1	1	1	0	1	1	1	1	1	1	0	1	13
Cell_percent	1	1	1	1	1	1	1	1	1	0	1	1	1	1	0	13
Entropy	1	1	1	0	1	1	1	1	0	1	1	0	1	0	1	11
Dissimilarity	1	1	1	1	1	1	0	1	0	1	1	1	0	0	1	11
Heights_short_axis	1	1	1	1	1	1	1	1	1	1	0	0	0	1	0	11
Homogeneity	1	1	1	0	1	1	0	1	0	1	1	0	1	0	1	10
PhaseVolume	1	1	1	0	1	1	0	1	1	1	0	1	0	1	0	10
Roi_count	0	0	1	0	0	1	1	0	1	1	1	1	1	1	1	10
Cell_grad	1	1	1	1	1	1	1	0	0	0	1	1	1	0	0	10
Perimeter	1	1	1	1	1	1	1	1	0	1	0	0	0	0	1	10
Skewness	1	1	1	1	0	0	1	1	1	0	1	0	1	0	0	9
Correlation	0	0	1	1	1	1	0	0	1	1	1	1	1	0	0	9
Bimodality	1	1	1	1	0	0	1	1	0	0	1	0	1	1	0	9
MCS	0	1	1	1	0	0	0	1	0	1	1	1	1	0	1	9
g	1	1	1	1	1	0	1	1	1	0	0	0	0	1	0	9
Surface_area	1	1	1	0	1	1	0	1	0	1	0	0	0	1	1	9
Mean2var	0	0	0	1	1	0	1	0	1	1	1	0	1	1	0	8
Mode	1	1	1	0	1	1	0	1	1	1	0	0	0	0	0	8
Slice_area	1	1	1	0	1	0	0	1	0	1	0	0	0	1	1	8
Volume	1	1	1	0	1	0	0	1	0	1	0	0	0	1	0	8
Adj_grad	1	0	1	1	0	1	0	0	0	0	1	1	0	1	1	8
Minor_axis_length	1	1	1	0	1	0	0	1	0	1	0	0	0	0	1	7
Stromal_grad	1	1	0	1	0	1	1	0	1	0	0	1	0	0	0	7
Kurtosis	1	0	1	1	1	0	1	0	0	0	0	1	0	0	0	6
Dist	1	1	0	1	0	1	1	0	1	0	0	0	0	0	0	6
Contrast	0	0	1	1	1	0	0	0	0	0	1	1	0	0	0	5
Major_axis_lenght	1	1	0	1	0	0	1	0	1	0	0	0	0	0	0	5
Eccentricity	1	1	0	1	0	0	1	0	1	0	0	0	0	0	0	5
Heights_long_axis	1	1	0	1	0	0	1	0	1	0	0	0	0	0	0	5
Perimeter_div_surf_area	1	1	0	1	0	0	1	0	1	0	0	0	0	0	0	5
Nb. of parameters which recognised classes as different	25	24	23	21	19	17	17	17	16	16	14	12	11	11	11	

blood cell segmentation [45], phenotypic cancer cell classification as epithelial or mesenchymal cell types [46], as well as the detection of pathogens [21]. Optical phase features extracted from the QPIs (such as phase volume, dry mass density, texture parameters, anisotropy) improved the cells' classification accuracy [47] and cancerous tissue detection [38], without chemicals for staining and with quick turnaround time. Automatic classification showed good performance metrics even when small data sets were used [48]. QPIs (either obtained by DHM or other phase methods such as SLIM) provide reproducible and unbiased quantitative biomarkers for cancer detection, as they are based on native physical attributes of the sample and are independent of staining or the techniques used for image acquisition and reconstruction.

In our study an extensive library of 614 QPIs obtained from unstained tissue samples collected from 18 patients, was created. It containes images for gliomas of grade II to IV and healthy tissue (40 images were identified by the pathologists as normal tissue and were situated peripherally to tumors). Various parameters characterizing the images were computed for entire and for specific areas of
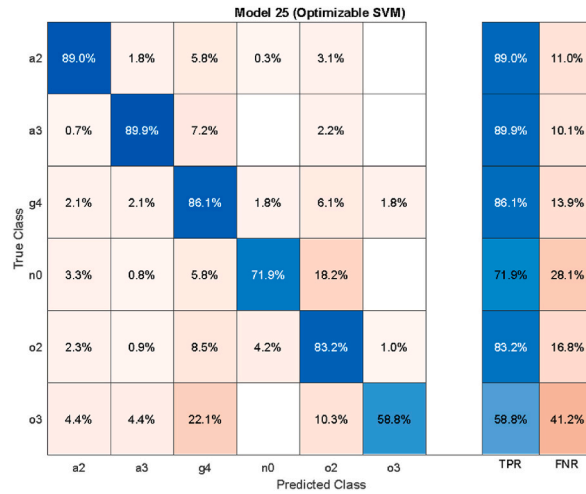
Fig. 5. Confusion matrix resulted from the training and validation step, using the Gaussian SVM (TPR = true positive rate, FNR = false negative rate).
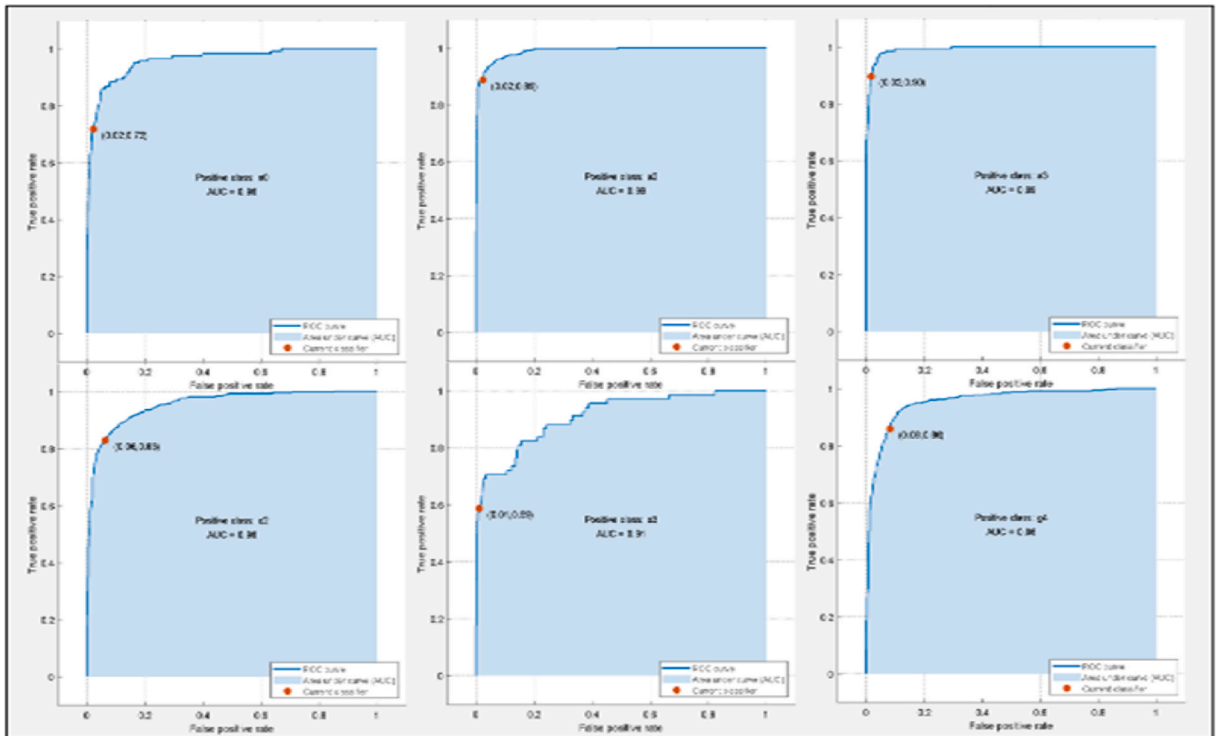

Fig. 6. ROC curves resulting from the training and validation step (using Gaussian SVM, *one-vs-all*).

QPIs and used as classifiers.

A Gaussian SVM was trained and validated on parameters from 75 % of the QPIs belonging to each class, then tested on a *naïve* set composed of the rest of 25 % of the images. The availability in the clinic of different tumor types limited the number of samples in each category. It resulted in an uneven number of images in each class. Although some recent publications consider the *one-vs-one* approach as being more suitable than *one-vs-all* strategy for tasks involving unbalanced classes [49], in our case the latter approach proved to be adequate, since the algorithm is facing a multi-grade pathology. This strategy is more useful in clinical practice because it can distinguish a certain class among the others.

The presented algorithm showed the highest sensitivity for a2, a3, and o2 classes, while as concerns the specificity, the highest values were obtained for o3, a2 and a3. It results that a2 and a3 are the classes for which the algorithm produced the most robust results

Table 3

Performance of classification on glioma images classes, obtained on the *naïve* set (TP = true positive, FN = false negative, TN = true negative, FP = false positive, PPV = positive predicted value, NPV = negative predicted value).

Classes	nb. of QPIs	TP	FN	TN	FP	Sensitivity	Specificity	PPV	NPV
n0	40	30	11	475	22	73 %	96 %	58 %	98 %
a2	109	90	18	415	13	83 %	97 %	87 %	96 %
a3	46	40	6	465	12	87 %	97 %	77 %	99 %
o2	191	164	27	465	37	86 %	93 %	82 %	95 %
o3	23	11	12	341	2	48 %	99 %	85 %	97 %
g4	205	170	35	335	23	83 %	94 %	88 %	91 %

(which can also be seen in the ROC curves).

Clinically, the grade IV glioma (g4 class in our study) and the grade III gliomas (subtypes a3 and o3) are often confused as they have common histological features (glioblastoma is a diffuse astrocytoma with mitotic activity, necrosis and microvascular proliferation, but it may have an oligodendroglial component too [6,50]). This explains why a study based on Raman spectroscopy (although powerful in determining specific molecular fingerprints) found difficult to classify these grades, and Zhou and col. [36] developed classifiers only for grade I-II versus grade III-IV.

There are algorithms for DP that have been developed using images of classical H&E and immunohistochemical stained tissue samples. Rathore and col. [51] classified gliomas in two classes (low grade I-II and high grade III-IV) by using six SVM models and various features. Despite the important number of images used for training the models, the authors are reporting accuracies lower than those of our study. When combined radiology and pathology images features were used, the deep learning-based algorithms managed to categorize diffuse gliomas (grade II) in two subtypes (oligodendroglioma and astrocytoma) with accuracies close to 90 % [52].

However, our algorithm can classify six classes (normal tissue and five glioma subtypes), with good sensitivity and specificity, including a3 and g4 (thus distinguishing between grades III and IV), and overcomes the difficulties faced by the pathologists when diagnosing the histological slide. This is a good argument for an extended use of quantitative phase images, which contain in each pixel information about the refractive index of the tissue, which, in turn, is directly related to the local protein content. It is well known that the progression to malignancy is associated to changes in the protein distribution and consequently to changes in "the nanoscale tissue architecture" [53,54].

In the case of o3, the lowest sensitivity was obtained. This result can be attributed to the reduced number of samples (which limited the number of samples available for training). Instead, a very good specificity in identifying this type of glioma was achieved. The algorithm mistakenly classified o3 QPIs as being g4 or o2 (5 and 4 QPIs out of 23, respectively). The confusion may be explained by the fact that o3 is the higher level of malignancy of o2 (sharing thus many morphological features), while g4 may have an oligodendroglial component.

The main advantages of the procedures used in this study are:

1) the images, as datasets, do not need special pre-processing steps like conversion to grayscale or color normalization, the latter being necessary in the case of classical histological images to minimize the influence of the preparation artifacts or of the color variation on the classification accuracy [55];
2) classifications based on QPIs analysis are more objective, being based on the protein content/distribution within the tissue, and less prone to misinterpretations;
3) samples don't need to be stained;
4) in principle, QPIs can be also acquired on fresh samples.

The following limitations have to be mentioned:

1) the image quality in terms of pixel phase values may be affected by the existence of paraffin traces; removing the paraffin must be done carefully;
2) algorithms' implementation in QPIs-based DP is hampered by the scarcity of libraries of phase images on which the algorithms should be trained; there is a need in increasing the clinicians' awareness about the advantages of these new label-free techniques and getting them involved in obtaining larger phase image libraries.

Quantitative phase imaging is a versatile technique in providing quantitative phase images not only by DHM, but also by other several techniques like: Spatial Light Interference Microscopy [56], White Diffraction Microscopy [57], and Gradient Light Interference Microscopy [58].

5. Conclusions

A SVM algorithm was developed to classify QPIs (obtained by DHM) of glioma samples according to WHO grading system. The algorithm uses a large collection of statistical, textural, and morphological parameters computed on QPIs from unstained samples and discriminates with high statistical accuracy between 5 subtypes of gliomas.

DHM, as provider of quantitative phase parameters, was confirmed as a valuable supporting-tool for digital pathology, complementary to the well-established methods (histopathology, immunohistochemistry). The objectivity of algorithms based on QPIs relies on the fact that they use information directly related to the morpho-biochemical modification of cells on their path to malignancy.

Our study contributes to the development of high-throughput computer aided methods for a faster and more accurate diagnostic in the support of pathologists.

6. Patents

Part of the procedure described in this paper has been patented under the number RO134410/2019 by the Romanian State Office for Inventions and Trademarks [59].

Ethics statement

The authors declare that the study complies with all regulations. The Ethics Committee at Bagdasar-Arseni Clinical Emergency Hospital approved the study (Institutional approval form no. 19747/May 25, 2021) and waived the requirement of informed consent.

Data availability statement

Data associated with this study have not been deposited into a publicly available repository. The datasets generated or analyzed during this study are available upon reasonable request.

CRediT authorship contribution statement

Violeta L. Calin: Writing – review & editing, Writing – original draft, Software, Methodology, Investigation, Formal analysis, Data curation, Conceptualization. **Mona Mihailescu:** Writing – review & editing, Writing – original draft, Methodology, Data curation, Conceptualization. **George E. D. Petrescu:** Writing – original draft, Investigation, Data curation. **Mihai Gheorghe Lisievici:** Investigation. **Nicolae Tarba:** Software, Formal analysis. **Daniel Calin:** Software, Formal analysis. **Victor Gabriel Ungureanu:** Software, Formal analysis. **Diana Pasov:** Investigation. **Felix M. Brehar:** Investigation. **Radu M. Gorgan:** Investigation. **Mihaela G. Moisescu:** Writing – review & editing, Writing – original draft, Methodology, Conceptualization. **Tudor Savopol:** Writing – review & editing, Writing – original draft, Methodology, Conceptualization.

Declaration of competing interest

The authors declare the following financial interests/personal relationships which may be considered as potential competing interests: Violeta L. Calin reports article publishing charges was provided by University of Medicine and Pharmacy Carol Davila. Violeta L. Calin, Mona Mihailescu reports equipment, drugs, or supplies was provided by Optoelectronica 2001 S.A. Violeta L. Calin, Mona Mihailescu, Tudor Savopol, Mihaela G. Moisescu have a patent licensed no. RO134410/2019 from Romanian State Office for Inventions and Trademarks.

References

[1] R. Leece, J. Xu, Q.T. Ostrom, et al., Global incidence of malignant brain and other central nervous system tumors by histology, 2003-2007, Neuro Oncol. 19 (11) (2017) 1553–1564.

[2] D.N. Louis, H. Ohgaki, O.D. Wiestler, et al., The 2007 WHO classification of tumours of the central nervous system, Acta Neuropathol. 114 (2) (2007) 97–109.

[3] Q.T. Ostrom, N. Patil, G. Cioffi, et al., CBTRUS statistical report: primary brain and other central nervous system tumors diagnosed in the United States in 2013-2017, Neuro Oncol. 22 (12 Suppl 2) (2020) iv1–iv96.

[4] Q.T. Ostrom, M. Price, C. Neff, et al., CBTRUS statistical report: primary brain and other central nervous system tumors diagnosed in the United States in 2015-2019, Neuro Oncol. 24 (Suppl 5) (2022) v1–v95.

[5] D.N. Louis, A. Perry, G. Reifenberger, et al., The 2016 World Health organization classification of tumors of the central nervous system: a summary, Acta Neuropathol. 131 (6) (2016) 803–820.

[6] A. Perry, P. Wesseling, Chapter 5 - Histologic Classification of Gliomas, Elsevier, 2016.

[7] S. Han, Y. Liu, S.J. Cai, et al., IDH mutation in glioma: molecular mechanisms and potential therapeutic targets, Br. J. Cancer 122 (11) (2020) 1580–1589.

[8] D.N. Louis, A. Perry, P. Wesseling, et al., The 2021 WHO classification of tumors of the central nervous system: a summary, Neuro Oncol. 23 (8) (2021) 1231–1251.

[9] D. Capper, D.T.W. Jones, M. Sill, et al., DNA methylation-based classification of central nervous system tumours, Nature 555 (7697) (2018) 469–474.

[10] M.D. Zarella, D. Bowman, et al., A practical guide to whole slide imaging: a white paper from the digital pathology association, Arch. Pathol. Lab Med. 143 (2) (2018) 222–234.

[11] K. Bera, K.A. Schalper, D.L. Rimm, et al., Artificial intelligence in digital pathology - new tools for diagnosis and precision oncology, Nat. Rev. Clin. Oncol. 16 (11) (2019) 703–715.

[12] A. Echle, N.T. Rindtorff, T.J. Brinker, et al., Deep learning in cancer pathology: a new generation of clinical biomarkers, Br. J. Cancer 124 (4) (2021) 686–696.

[13] Y. Park, C. Depeursinge, G. Popescu, Quantitative phase imaging in biomedicine, Nat. Photonics 12 (10) (2018) 578–589.

[14] Depeursinge C. D., Cuche E., Colomb T et al., Cells and tissue imaging with digital holographic microscopy, Proc. SPIE (2003) 5143_134.

[15] P. Memmolo, G. Aprea, V. Bianco, et al., Differential diagnosis of hereditary anemias from a fraction of blood drop by digital holography and hierarchical machine learning, Biosens. Bioelectron. 201 (2022) 113945.

[16] E. Scarlat Mihailescu M., I. Paun, M. Scarlat, Discriminating the main representatives of the white blood cell species on the basis of the fractal properties of the DHM phase profile, U.P.B. Sci. Bull. Series A 75 (2) (2013).

[17] D. Roitshtain, L. Wolbromsky, E. Bal, et al., Quantitative phase microscopy spatial signatures of cancer cells, Cytometry 91 (5) (2017) 482–493.

[18] V.L. Calin, M. Mihailescu, E.I. Scarlat, et al., Evaluation of the metastatic potential of malignant cells by image processing of digital holographic microscopy data, FEBS Open Bio (2017) 1527–1538.

[19] P. Jourdain, F. Becq, S. Lengacher, et al., The human CFTR protein expressed in CHO cells activates aquaporin-3 in a cAMP-dependent pathway: study by digital holographic microscopy, J. Cell Sci. 127 (Pt 3) (2014) 546–556.

[20] M. Ugele, M. Weniger, M. Leidenberger, et al., Label-free, high-throughput detection of P. falciparum infection in sphered erythrocytes with digital holographic microscopy, Lab Chip 18 (12) (2018) 1704–1712.

[21] T. O'Connor, B. Javidi, COVID-19 screening with digital holographic microscopy using intra-patient probability functions of spatio-temporal bio-optical attributes, Biomed. Opt Express 13 (10) (2022) 5377–5389.

[22] A. Yakimovich, R. Witte, V. Andriasyan, et al., Label-free digital holo-tomographic microscopy reveals virus-induced cytopathic effects in live cells, mSphere 3 (6) (2018) e00599–18.

[23] Dubey V., Ahmad A., Singh R., et al., Digital holographic microscopy and machine learning approach for the classification of inflammation in macrophages, OSA Technical Digest (2019) paper Th3A.4.

[24] P. Jourdain, N. Pavillon, C. Moratal, et al., Determination of transmembrane water fluxes in neurons elicited by glutamate ionotropic receptors and by the cotransporters KCC2 and NKCC1: a digital holographic microscopy study, J. Neurosci. 31 (33) (2011) 11846–11854.

[25] V.L. Calin, M. Mihailescu, N. Tarba, et al., Digital holographic microscopy evaluation of dynamic cell response to electroporation, Biomed. Opt Express 12 (4) (2021) 2519–2530.

[26] Z. El-Schich, A. Leida Mölder, A. Gjörloff Wingren, Quantitative phase imaging for label-free analysis of cancer cells—focus on digital holographic microscopy, Appl. Sci. 8 (7) (2018) 1027.

[27] Z. El-Schich, Digital holographic microscopy: a noninvasive method to analyze the formation of spheroids, Biotechniques 71 (6) (2021) 598–603.

[28] V.L. Calin, M. Mihailescu, N. Mihale, et al., Changes in optical properties of electroporated cells as revealed by digital holographic microscopy, Biomed. Opt Express 8 (4) (2017) 2222–2234.

[29] P. Marquet, B. Rappaz, P.J. Magistretti, et al., Digital holographic microscopy: a noninvasive contrast imaging technique allowing quantitative visualization of living cells with subwavelength axial accuracy, Opt Lett. 30 (5) (2005) 468–470.

[30] A. Bokemeyer, P.R. Tepasse, L. Quill, et al., Quantitative phase imaging using digital holographic microscopy reliably assesses morphology and reflects elastic properties of fibrotic intestinal tissue, Sci. Rep. 9 (1) (2019) 19388.

[31] R. Barer, Refractometry and interferometry of living cells, J. Opt. Soc. Am. 47 (6) (1957) 545–556.

[32] M. Hellesvik, H. Øye, H. Aksnes, Exploiting the potential of commercial digital holographic microscopy by combining it with 3D matrix cell culture assays, Sci. Rep. 10 (1) (2020) 14680.

[33] M. Mihailescu, E.I. Scarlat, I.A. Paun, et al., Empirical quantitative characterization of holographic phase images of normal and abnormal cervical cells by fractal descriptors, Comput. Methods Biomech. Biomed. Eng.: Imaging & Visualization 6 (4) (2018) 386–395.

[34] C. Krafft, K. Thümmler, S.B. Sobottka, et al., Classification of malignant gliomas by infrared spectroscopy and linear discriminant analysis, Biopolymers 82 (4) (2006) 301–305.

[35] S. Nandy, M. Sanders, Q. Zhu, Classification and analysis of human ovarian tissue using full field optical coherence tomography, Biomed. Opt Express 7 (12) (2016) 5182–5187.

[36] Y. Zhou, C.-H. Liu, B. Wu, et al., Optical biopsy identification and grading of gliomas using label-free visible resonance Raman spectroscopy, J. Biomed. Opt. 24 (9) (2019) 095001.

[37] Z. Wang, K. Tangella, A. Balla, et al., Tissue refractive index as marker of disease, J. Biomed. Opt. 16 (11) (2011) 116017–1160177.

[38] J.K. Zhang, Y.R. He, N. Sobh, et al., Label-free colorectal cancer screening using deep learning and spatial light interference microscopy (SLIM), APL, Photonics 5 (4) (2020) 040805.

[39] S. Ortega, H. Fabelo, R. Camacho, et al., Detecting brain tumor in pathological slides using hyperspectral imaging, Biomed. Opt Express 9 (2) (2018) 818–831.

[40] V.L. Calin, G.E.D. Petrescu, M. Mihailescu, et al., P04.17 differential diagnosis of gliomas using digital holographic microscopy, Neuro Oncol. 21 (Suppl 3) (2019) iii32–iii33.

[41] Calin V. L, Mihailescu M., Costea R. V. et al., Optical biomarkers for detection of malignant tissue using Digital Holographic Microscopy, Proc. SPIE EB101 (2019) 11076_39.

[42] T. Colomb, E. Cuche, F. Charrière, et al., Automatic procedure for aberration compensation in digital holographic microscopy and applications to specimen shape compensation, Appl. Opt. 45 (5) (2006) 851–863.

[43] R.M. Haralick, K. Shanmugam, I. Dinstein, Textural features for image classification, IEEE Transactions on Systems, Man, and Cybernetics SMC-3 (6) (1973) 610–621.

[44] S. Sridharan, V. Macias, K. Tangella, et al., Prediction of prostate cancer recurrence using quantitative phase imaging, Sci. Rep. 5 (1) (2015) 9976.

[45] T. O'Connor, A. Anand, B. Andemariam, et al., Deep learning-based cell identification and disease diagnosis using spatio-temporal cellular dynamics in compact digital holographic microscopy, Biomed. Opt Express 11 (8) (2020) 4491–4508.

[46] V. Lam, T. Nguyen, V. Bui, et al., Quantitative scoring of epithelial and mesenchymal qualities of cancer cells using machine learning and quantitative phase imaging, J. Biomed. Opt. 25 (2) (2020) 1–17.

[47] A. Cohen, M. Dudaie, I. Barnea, et al., Label-free imaging flow cytometry for cell classification based on multiple interferometric projections using deep learning, Advanced Intelligent Systems 6 (2300433) (2023) 1–11.

[48] M. Rubin, O. Stein, N.A. Turko, et al., TOP-GAN: stain-free cancer cell classification using deep learning with a small training set, Med. Image Anal. 57 (2019) 176–185.

[49] J.A. Gualtieri, R. Cromp, [Support Vector Machines for Hyperspectral Remote Sensing Classification] SPIE, AI, 1999.

[50] M. Yao, S. Li, X. Wu, et al., Cellular origin of glioblastoma and its implication in precision therapy, Cell. Mol. Immunol. 15 (8) (2018) 737–739.

[51] S. Rathore, T. Niazi, M.A. Iftikhar, et al., Glioma grading via analysis of digital pathology images using machine learning, Cancers 12 (3) (2020) 578.

[52] T. Kurc, S. Bakas, X.H. Ren, et al., Segmentation and classification in digital pathology for glioma research: challenges and deep learning approaches, Front. Neurosci. 14 (2020) 15.

[53] H. Majeed, M.E. Kandel, K. Han, et al., Breast cancer diagnosis using spatial light interference microscopy, J. Biomed. Opt. 20 (11) (2015) 111210.

[54] Y. Liu, S. Uttam, S. Alexandrov, et al., Investigation of nanoscale structural alterations of cell nucleus as an early sign of cancer, BMC Biophys. 7 (1) (2014) 1.

[55] S.M. Ayyad, M. Shehata, A. Shalaby, et al., Role of AI and histopathological images in detecting prostate cancer: a survey, Sensors 21 (8) (2021) 2586.

[56] X. Chen, M.E. Kandel, G. Popescu, Spatial light interference microscopy: principle and applications to biomedicine, Adv. Opt Photon 13 (2) (2021) 353–425.

[57] T. Kim, R. Zhou, M. Mir, et al., White-light diffraction tomography of unlabelled live cells, Nat. Photonics 8 (3) (2014) 256–263.
[58] T.H. Nguyen, M.E. Kandel, M. Rubessa, et al., Gradient light interference microscopy for 3D imaging of unlabeled specimens, Nat. Commun. 8 (1) (2017) 210.
[59] Mona Mihailescu, Violeta Liuba Calin, Georgeta Mihaela Moisescu, Tudor Savopol, Process for Classifying Malignancy Degree of Tissue Biopsy Samples by Digital Holographic Microscopy, patent OSIM RO134410, Romania, 2019.